



HAL
open science

In-situ 3D characterization of tensile damage mechanisms in A319 aluminium alloy using X-ray tomography and digital volume correlation

Zaidao Li, N. Limodin, Amina Tandjaoui, Philippe Quaegebeur, Jean-François Witz, David Balloy

► **To cite this version:**

Zaidao Li, N. Limodin, Amina Tandjaoui, Philippe Quaegebeur, Jean-François Witz, et al.. In-situ 3D characterization of tensile damage mechanisms in A319 aluminium alloy using X-ray tomography and digital volume correlation. *Materials Science and Engineering: A*, 2020, 794, pp.139920. 10.1016/j.msea.2020.139920 . hal-02933501

HAL Id: hal-02933501

<https://hal.science/hal-02933501v1>

Submitted on 8 Sep 2020

HAL is a multi-disciplinary open access archive for the deposit and dissemination of scientific research documents, whether they are published or not. The documents may come from teaching and research institutions in France or abroad, or from public or private research centers.

L'archive ouverte pluridisciplinaire **HAL**, est destinée au dépôt et à la diffusion de documents scientifiques de niveau recherche, publiés ou non, émanant des établissements d'enseignement et de recherche français ou étrangers, des laboratoires publics ou privés.

This paper has been and accepted and published in

Materials Science and Engineering: A

Volume 794, 9 September 2020

<https://doi.org/10.1016/j.msea.2020.139920>

In-situ 3D characterization of tensile damage mechanisms in A319 aluminium alloy using X-ray tomography and digital volume correlation

Zaidao Li ^{a,b,*}, Nathalie Limodin ^a, Amina Tandjaoui ^a, Philippe Quaegebeur ^a, Jean-François Witz ^a, David Balloy ^b

^a Univ. Lille, CNRS, Centrale Lille, FRE 2016 - LaMcube – Laboratoire de mécanique multiphysique et multiéchelle, F-59000 Lille, France

^b Univ. Lille, CNRS, INRA, ENSCL, UMR 8207 - UMET - Unité Matériaux et Transformations, F-59000 Lille, France

Abstract: Tensile tests with 3D in-situ observation were performed using X-ray tomography on a solution heat treated Lost Foam Cast A319 alloy. In-situ tensile testing allowed crack initiation and propagation to be visualised in 3D whilst the digital volume correlation technique was used to measure 3D deformation fields. Crack initiation mechanisms and the evolution of damage during crack growth together with the localized strains at the onset of cracks were studied in 3D. The results show that cracks initiate at hard inclusions, i.e. eutectic Si, iron intermetallics and Al₂Cu intermetallic phase, in the vicinity of large pores under the influence of their strain concentration. Once initiated, cracks appeared to preferentially grow through the cracked hard inclusions. Quantitative analysis revealed that the average strain level for the failure of iron-intermetallics exhibits lower value than for Al₂Cu intermetallic phase. Besides, final fracture was more prone to occur at Si phase, iron intermetallics and Al₂Cu intermetallic phases than Al dendrites. For the various hard inclusions, failure predominantly occurred by fracture rather than decohesion.

Keywords: Damage, A319, Digital Volume Correlation, in situ tensile test, X-ray tomography

1 Introduction

Aluminium-silicon (Al-Si) alloys are now extensively used in various automotive components such as cylinder heads because of their light weight in addition to a range of desirable engineering properties. In automotive industry, Lost Foam Casting (LFC) process is progressively replacing gravity Die Casting (DC) process because of geometry optimization and cost reduction [1]. However, a major disadvantage of Lost Foam Casting is the relatively coarse microstructure compared to die casting processes with higher cooling rates [2]. This coarse microstructure consists of hard second phase particles (eutectic Si, Al₂Cu intermetallic phase, and iron-intermetallics), large pores and microshrinkage cavities that significantly influence the castings performance [3]. It is thus important to identify the damage mechanisms of the LFC Al-Si alloy in relationship with the microstructure.

Pores, as preferential crack nucleation sites, are often the main cause of the poor tensile/fatigue properties exhibited by Al-Si components [4,5]. In particular, large surface pores play a decisive role in providing preferential crack initiation sites by creating a high stress concentration in the matrix nearby during monotonic tensile and cyclic loadings [6]. Hard inclusions, such as eutectic Si, iron-intermetallics and Al₂Cu intermetallic phase, also play an important role on the tensile/fatigue behaviour.

Under monotonic loading, cracks appear more likely to occur through the fracture of iron-intermetallics in a high-Fe A319 alloy, and propagate through the fracture of Al₂Cu, as well as through that of brittle Si particles [7]. The fracture path primarily goes through the largest Si particles in an AlSi7Mg0.3 (A356) alloy [8] and Si particles tend to break in a direction perpendicular to the stress [9]. Joseph et al. [10] used the polarized Raman technique to estimate failure stress of Si in an Al-Si alloy subjected to different heat treatments. The values obtained, which range between 500 and 1000 MPa, depend on particle morphology, *i.e.* an unmodified Si particle breaks at a lower stress than a modified hence more globular particle; The smallest spherical particles do not break [10].

In some cases, intermetallics are reported not to fail because of their higher thickness or greater resistance as compared to eutectic Si [9]. However, there are almost no quantitative studies on the iron-intermetallics and Al₂Cu intermetallic phase rupture. Cantor et al. [11] found that the rupture of an Al-Al₂Cu eutectic alloy occurs at a deformation of 0.87 % at room temperature. The influence of the Fe

content is studied only through the evolution of macroscopic mechanical properties (increase of the elastic limit and of the maximum tensile strength, reduction of the ductility) [12].

Some authors [13–15] also studied the changes in microstructure and properties of Al-Si-Cu alloy after heat treatment. Usually, in order to avoid incipient melting of the copper-rich phase that would introduce micro pores, the temperature used in conventional solution treatment for Al-Si-Cu alloys is restricted to 495°C [16]. Nevertheless, Toda et al. [15] studied the dissolution of the Al₂Cu intermetallic phase for different solution treatments of Al-Si-Cu alloys and reported the positive effect of a high-temperature solution treatment, i.e. 534°C, on the tensile strength.

Most of the above studies are based on 2D/surface observation. In recent years, X-ray microtomography has been employed to visualise the 3D distribution of internal defects and cracks in bulk metal materials [17–19]. In some cases, the three-dimensional tomography images can be analysed with Digital Volume Correlation (DVC) to evaluate 3D displacement fields near the crack tip in a loaded specimen [2,20]. In addition, although the damage mechanisms of as-cast LFC A319 alloy studied in [6] revealed the important role of pores by 3D analysis, the influence of different hard inclusions on these damage mechanisms, especially after a solution heat treatment, are still not clear and require further study.

In this study, a solution heat treatment process was performed on an Al-Si-Cu alloy to achieve a lower volume fraction of the Al₂Cu intermetallic phase. Then, in order to investigate the influence of the microstructure on the damage mechanisms in 3D, an experimental protocol was developed using X-ray tomography and DVC. The damage mechanisms of the LFC A319 samples after the solution heat treatment were investigated by 3D in-situ tensile testing. Crack initiation mechanisms and the evolution of damage during crack growth together with the local strains at the onset of cracks were studied in 3D. Quantitatively assessing the local strain at particles before their failure could help understanding differences in the damage mechanisms of the various hard inclusions.

2 Materials and methods

2.1 Material and Specimens preparation

The material used in this work was a LFC A319 alloy whose chemical composition is given in Table 1. The microstructure consists of α -Al, hard inclusions (eutectic Si, Al₂Cu intermetallic phase, α -AlFeSi, β -AlFeSi) and pores [21].

Table 1: Chemical composition of the experimental A319 alloy (wt. %)

Al	Si	Cu	Fe	Mn	Sr	Mg	Ti	Ni	Pb	Zn	Sn	Zr,V,P	
												each	total
bal.	7.85	3.05	0.30	0.190	0.0120	0.28	0.098	0.018	<0.015	0.16	<0.015	≤ 0.03	≤ 0.1

All specimens (30 in total) were extracted from the fire deck area (Figure 1), which is the most critical area of the cylinder head in regard to the thermomechanical loading. Figure 1(a) shows the extraction area in an A319 prototype cylinder head manufactured using LFC process.

2.3 3D microstructure characterization and in-situ tensile test

In order to characterize the microstructure, i.e. pores, Al₂Cu intermetallic phase, iron-intermetallics, in 3D, high resolution (voxel size of 2 μm) Lab-CT was performed on the ROI of specimens before in-situ tensile test. These high-resolution images enable to analyse the size, shape and spatial distribution of the microstructure. The main parameters used to characterize the morphology of pores and Al₂Cu intermetallic phase are Feret diameter, sphericity and volume. Feret diameter is defined as the longest distance measured between two parallel tangents on each side of the 3D object of interest [6]. It was used to assess the size of pores. Sphericity corresponds to the ratio between the object volume and the volume of a sphere with the same surface as the object in 3D. These 3D images obtained were processed and analyzed using ImageJ/Fiji and Avizo Fire softwares; One can refer to reference [12] for details regarding the method of analysis. Then, in-situ 3D tensile tests were performed on the heat-treated specimens using an in-situ tensile test rig (Figure 2).

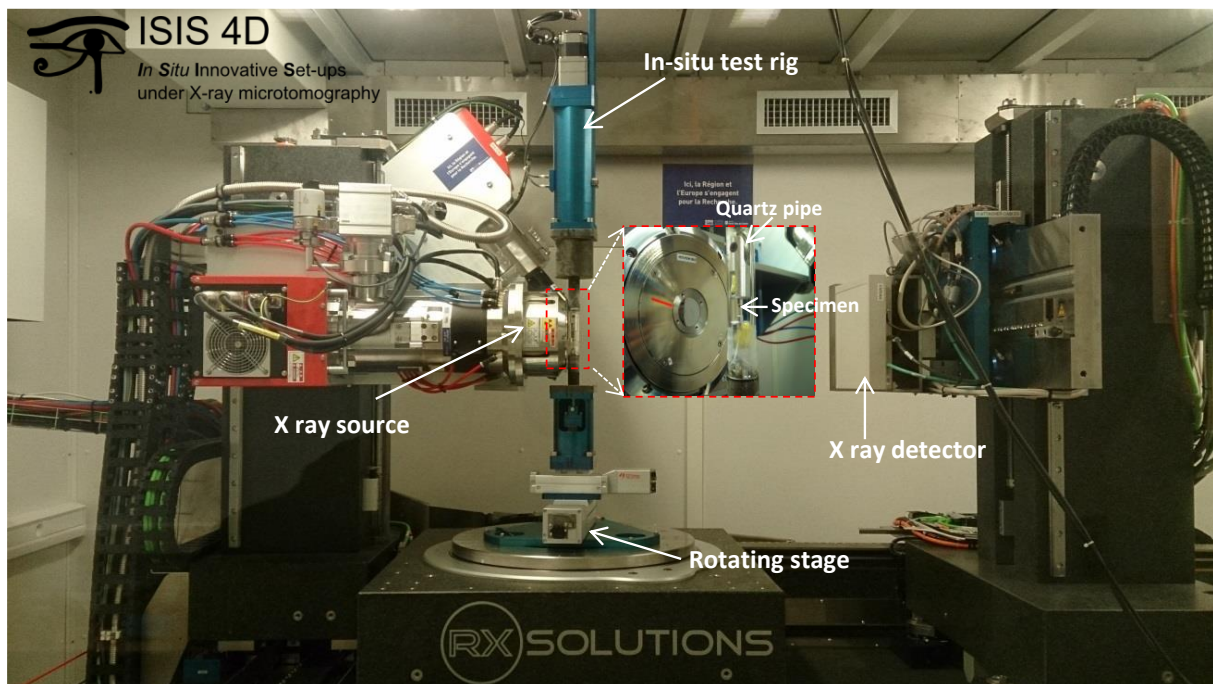


Figure 2: In-situ 3D tensile test set-up at ISIS4D

The four sides and corners of the tensile specimens were ground to ensure that all the surfaces are smooth and prevent the generation of stress concentration in order to minimize the possibility of crack initiation from machining marks. In addition, both “flat” surfaces, *e.g.* the front and back faces of the specimen shown in Figure 4, were ground and fine polished using standard metallurgical techniques for post-mortem analysis with Scanning Electron Microscopy (SEM).

The in-situ machine was mounted onto the rotating stage of the tomography system. A quartz tube allowed 360° rotation without hiding the specimen from the beam (see Figure 2), and it gave a constant and negligible attenuation of the X-ray photons. A force sensor was used to record the applied load in real time during the tests performed in displacement control at a speed of 1 μm/s. Preliminary tensile tests, without interruption for image acquisition, were performed on unsuitable specimens to define the loading step for the following tensile tests. The aim was to obtain several images at different loads between the elastic limit and the ultimate tensile strength to study damage evolution. Thus, 3D tomography images were taken from the selected ROI before any loading and at each load step when the test was interrupted, the specimen was loaded step by step until fracture.

In order to obtain an image with enough visible markers for DVC and to detect cracks, a high resolution is necessary, thus a voxel size of about 3 μm was chosen. The size of the scanned volume or ROI was 750×760×1300 voxels (2250×2280×3900 μm³). For each loading step, 1024 projections were taken

while the sample rotated over 360° about its longitudinal axis; the total scan time was equal to 33 min. After failure, a scan was also performed on one half of the broken specimen for each tensile test to analyse the 3D fracture surface.

2.4 Digital Volume Correlation (DVC)

In this study, displacement and strain field were measured with YaDICs software [23] using an isotropic element size of 8×8×8 voxels. This platform is based on C++ and it has been proven to be appropriate for the correlation of large 3D volumes [20].

The principle of DVC is to find the transformation between a fixed image and a moving one for a given metric or correlation criterion using an optimization scheme. As shown in Figure 3, in order to identify the transformation, several steps are necessary: define a correlation criterion, choose a sampling and an interpolator, then an optimizer and finally a regularization method [7].

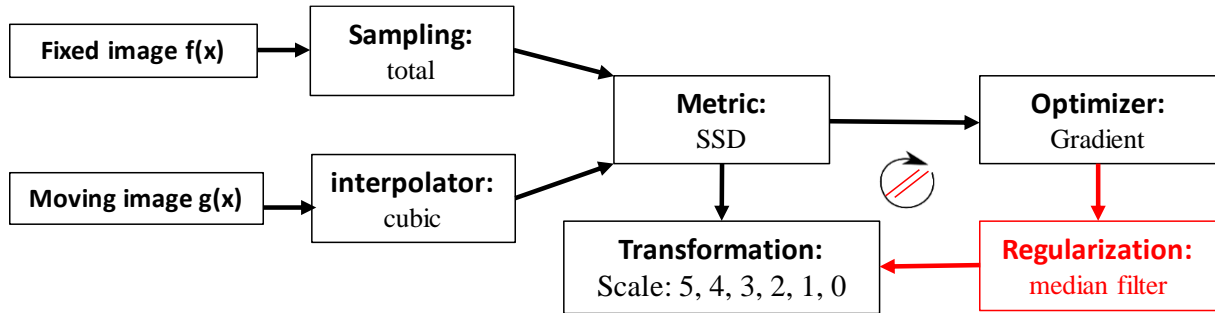


Figure 3: The basic registration components of YaDICs [23] image correlation platform at LaMcube laboratory.

In the present case, global (rigid and homogeneous) and elastic transformation were chosen so as to compute the Sum of Squared Difference (SSD) correlation criterion selected. The correlation criterion was evaluated on the total image. The gradient descent was used as optimizer method; the gradient of the correlation criterion was computed regarding the transformation parameters by:

$$\frac{\partial SSD}{\partial \mathbf{u}} = \frac{2}{\Omega} \sum_{\mathbf{x} \in \Omega} (f(\mathbf{x}) - g(\mathbf{x} + \mathbf{u}(\mathbf{x}))) \frac{\partial g(\mathbf{x} + \mathbf{u}(\mathbf{x}))}{\partial \mathbf{u}}$$

where $f(\mathbf{x})$ and $g(\mathbf{x})$ are the grayscale values of the reference and the deformed images respectively, Ω represents the integration area, \mathbf{x} is the vector indicating the position of any voxel, \mathbf{u} is the displacement vector for each position \mathbf{x} .

Then, a bi-cubic interpolator is used to apply the transformation to the moving images at each iteration. The correlation between the deformed and the reference images is based on a multiscale resolution strategy as a pyramid scheme. The transformation may be different at each scale: homogeneous deformation is searched for at the coarsest scales while at finer scales, local deformations are looked for at the nodes of a FE-like grid whose spacing gets finer and finer until the last scale is reached, i.e. the full resolution image. In the present work, six scales were used, the coarsest one is “scale 5” where one “macro” voxel is averaged over $2^5 \times 2^5 \times 2^5$ pixels, while the full resolution image corresponds to “scale 0”. The analysis sequence used was “OFI_RB, OFI_H, IC, OFFEM8, OFFEM8, OFFEM8” for scales 5–0.

- OFI_RB corresponds to an Optical Flow Integrated (OFI) method dedicated to rigid body motion (RB) computation.
- OFI_H also corresponds to an OFI method but it assumes a Homogeneous (H) deformation such as rigid body motions, i.e. translations and rotations, and global strains.

- IC corresponds to an Inter-Correlation method, which is based on Normalized Cross Correlation (NCC).
- OFFEM is an Optical Flow elastic transformation based on Finite Element Methods; it is used for the elastic deformation, because it has a good spatial coherence. OFFEM8 means the used element size is $8 \times 8 \times 8$ “macro” voxels.

DVC was performed between the reference image before load and the deformed image at each load step during the tensile test. In order to reduce the duration of the calculation, the displacement and strain fields were computed on a subvolume ($2190 \times 2190 \times 2190 \mu\text{m}^3$) of the ROI that contains all the cracks observed during the tensile test and the final fracture path. Uncertainty analysis was used to quantify the performances of DVC. It is estimated from the standard deviation of the displacement field measured between two images, one at a reference position and another one after a small translation [2]. In the present case, the DVC measurement uncertainty method can be described as follows: The X-ray tomography scan was performed on the specimen at a reference position, and then another scan was taken after a translation along the beam direction. As the lab-CT X-ray beam is conical, the voxel size will change from $3.05 \mu\text{m}$ to $3 \mu\text{m}$ in the present case after a translation along the beam direction, and then a known displacement field in all directions, i.e. a dilatation, which correspond to a maximum displacement of 15 voxel, was applied. Then, the standard deviation of the displacement is calculated for the three different directions and used to verify if there is one favored direction in the noise. The reader is referred to Ref. [7,20,24] for the more details of the DVC analysis procedure.

2.5 Post mortem analyses

Post mortem analyses were performed on the failed specimens using a HITACHI 3600N SEM in order to observe the microcracks and the microstructure on both flat surfaces, and to analyse the microstructural constituents in the fracture surfaces. X-ray Energy Dispersive Spectroscopy (EDS) was performed using the NORAN System SIX X-ray Microanalysis System. In order to identify the damage mechanisms of hard inclusions, EDS X-ray mappings were performed on all the fracture surfaces of tensile specimens using the analysis method reported in [22]. Each obtained elemental map for the lower and upper sides of the fracture surface is registered on the same area of the BSE image on one side of the fractured specimen in order to observe the relations between the fracture surface features and the distribution of the constituents. If the same constituent is identified in the same location on both sides of the fracture surface for one specimen, the failure mechanism of the corresponding hard particle is fracture. Otherwise, the failure mechanism is decohesion.

3 Results

3.1 Selection of ROI

In this study, FE simulations were performed using lab-CT images on the “suitable” specimens defined in section 2.1. The selection process of a ROI in one studied specimen for the in-situ tensile test observations is illustrated in Figure 4. Some studies [6,21] show that pores may generate enough strain localization zones for crack initiation during tensile loading. Thus, as shown in Figure 4(a), a microstructurally realistic mesh of the microstructure within the pristine sample (pores + matrix) was generated based on 3D image obtained by lab-CT. In this studied specimen, numerous large pores were found in the central region. Figure 4(b) shows the volumetric tetrahedral grid that was refined on the pores and specimen’s sharp corners. Then, the cumulated plastic strain distribution was computed and plotted by Abaqus software to identify potentially critical areas, i.e. the areas where the largest strain occurs (Figure 4(c)). The blue dotted box defines the ROI, which was used for 3D microstructural characterization in high resolution tomography and in-situ tensile test observation.

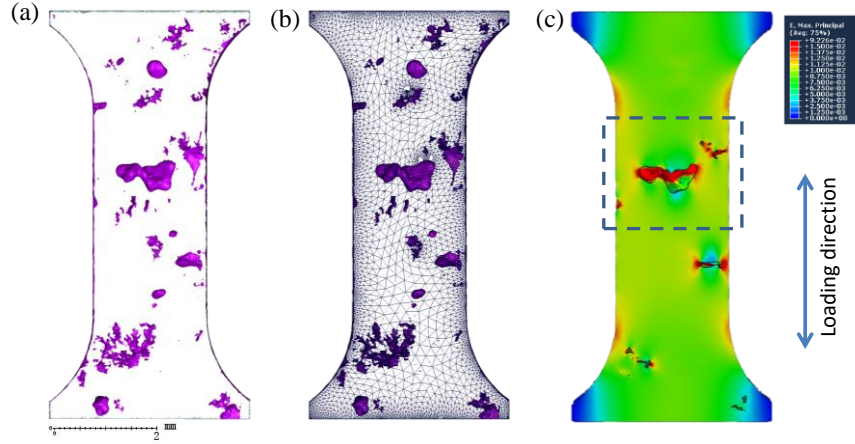


Figure 4: (a) 3D rendering of pores with Avizo software for one studied specimen, (b) 3D volume mesh, (c) FE calculation with Abaqus software showing ϵ_{zz} along the loading direction z in a slice which is 1.31 mm below the surface

3.2 Tensile tests with 3D in-situ observation

Three tensile tests with 3D *in situ* observation were performed. As the observed mechanisms were reproducible among these tests, only one specimen (shown in Figure 4) is presented in this paper. Interrupted tensile tests under Lab-CT were performed step by step until final failure, and most of the scans were acquired above the yield strength and slightly below the ultimate tensile strength in order to better observe the crack growth; the studied specimen failed in the ROI at a normal stress of 187 MPa.

Figure 5(a) shows an uncertainty of the DVC displacement field that ranges from about 0.21 voxel (0.65 μm) to 0.71 voxel (2.1 μm) for element sizes ranging from 32 to 8 voxels (96–24 μm). Although subvoxel, these uncertainty values are high when compared to what was achieved in [9] for the same material under synchrotron X-ray tomography. In the present study, fewer markers are indeed visible for DVC as eutectic Si is not revealed in Lab-CT images hence the higher DVC uncertainty. However, as a high spatial resolution is required to assess local deformation, elements with an 8 voxel edge were chosen as a good compromise between displacement uncertainty and spatial resolution of the displacement fields. For the selected size of elements, the maximum displacement uncertainty was assessed to be about 0.71 voxel. The average strains in the subvolume were calculated from DVC displacement fields for each loading step to draw the stress-strain curve (“A319 *in situ* test” in Figure 5) for this in-situ test. As shown in Figure 5(b), the stress-strain curve so measured is a little below that of a standard test. The reason can be that the small DVC analysis volume, which contains almost all the large pores and main cracks, shows higher mean strain value than a standard test, i.e. with extensometer measurement, on a larger specimen. Therefore, the results confirmed that DVC measurements could be considered reliable.

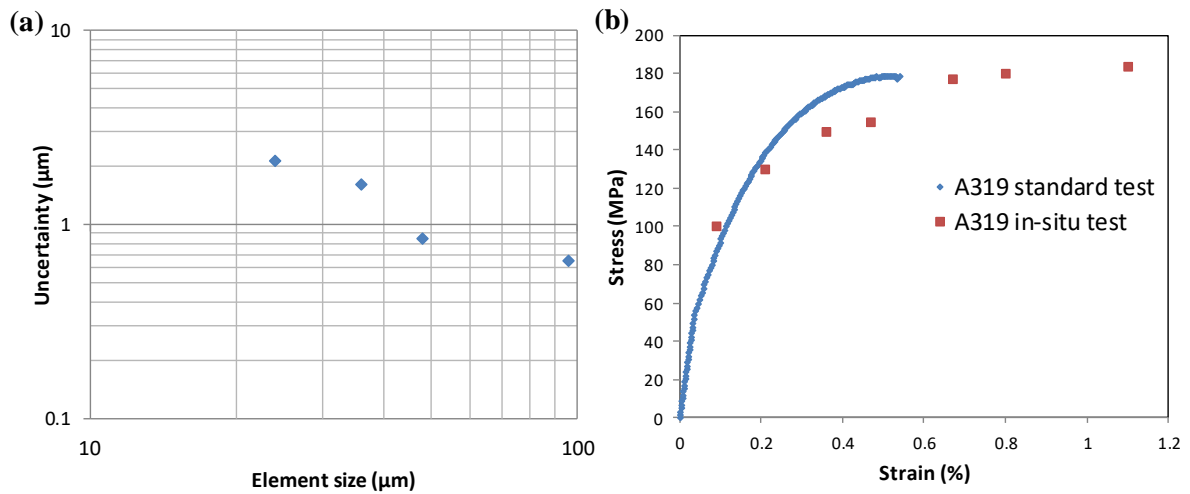


Figure 5 : (a) Uncertainty in the displacement measured by DVC as a function of element size, and (b) Stress-strain curve deduced from DVC measurement for the studied specimen shown in Figure 4 and from a standard test performed on LFC A319 alloy

The final failure occurred through a cluster of pores. As shown in Figure 6, three large pores, i.e. pores A, B and C, were observed on the fracture surface; the measured strain fields along the loading direction are superimposed on the 3D rendering of the fracture surface.

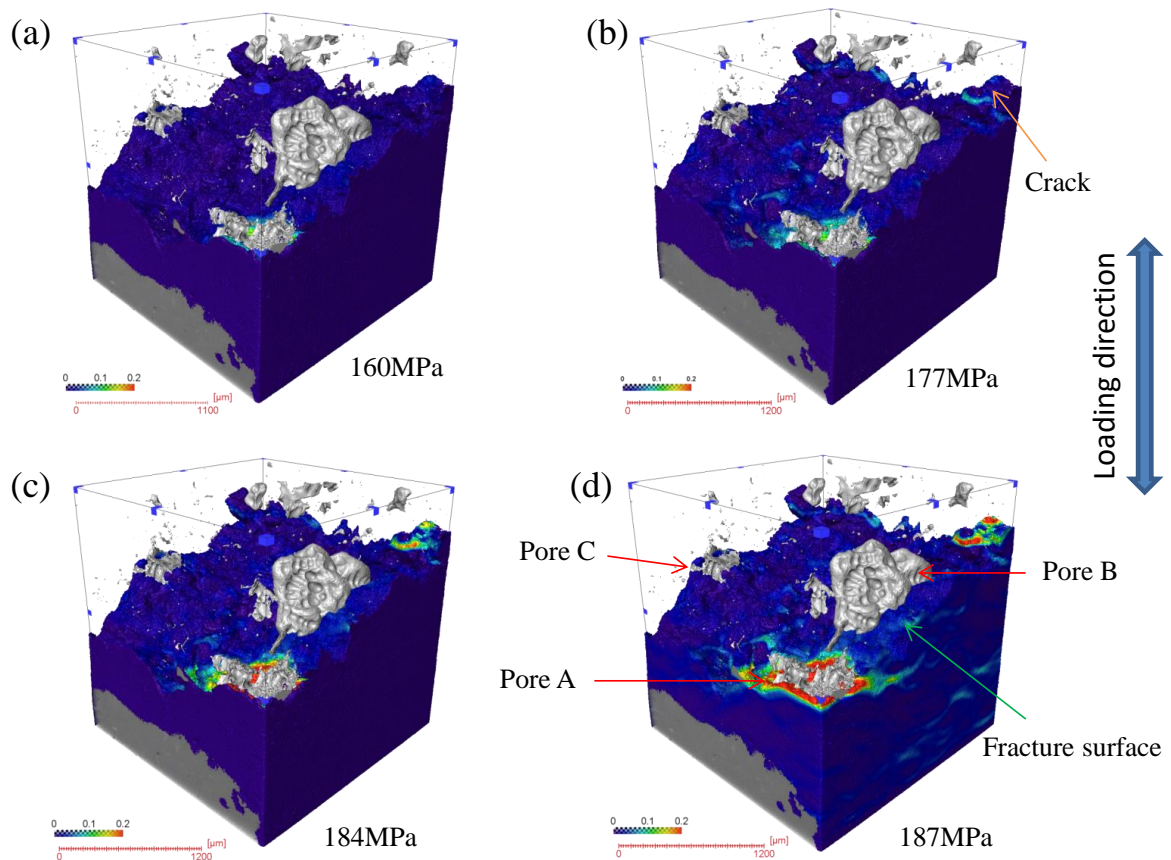


Figure 6: 3D rendering of pores on the fracture surface of the studied specimen, the ϵ_{zz} strain calculated by DVC for different loading steps, (a) 160MPa, (b) 177MPa, (c) 184MPa and (d) 187MPa, are superimposed on the fracture surface

In Figure 6, Pores A, B and C, the three largest pores, occupy 83 % of all the pores volume in the ROI while other pores have Feret diameter smaller than 511 μm ; their main parameters are given in Table 2.

Table 2: Parameters of the pores on the fracture surface of the studied specimen

Pore	Feret diameter (μm)	Volume (mm^3)	Sphericity (F)	Type	Region
A	842	0.0177	0.078	Surface pore	Crack initiation and growth zone
B	1176	0.0976	0.422	Subsurface pore	
C	523	0.0037	0.164	Surface pore	Final failure zone

The tomography images analysis allows observing small cracks around surface shrinkage Pore A at an applied stress of 160 MPa (Figure 6(a)), while only one small crack was observed around the subsurface Pore B before the last loading step, although it is the largest pore.

Although only a small crack nucleated around Pore B, and no crack was observed around Pore C before the final fracture, they are likely to have an influence on fracture damage by increasing the stress concentration around Pore A, which is located in the same plane perpendicular to the loading direction, hence facilitating the final fracture. Another main crack (see yellow arrow in Figure 6(b)) initiated close to the corner of the specimen at an applied stress of 177 MPa, and then it grew with a further increase in the applied stress. As shown in Figure 6, two high strain locations, which correspond to the visible cracks, were observed in the area around Pore A and in the corner of specimen. However, it should be noted that the large deformations in Figure 6(c) and (d) around cracks are caused by crack opening instead of by real deformation.

SEM-EDS analysis (Figure 7) was performed on the fracture surface of specimen. The areas where the cracks were observed to initiate and grow during the in-situ tensile test were marked by dotted box in Figure 7(a) and (c). They are named accordingly with the three main cracks, presented hereafter, that were detected from the slice by slice analysis of the tomographic images at different loading steps.

Quantitative analyses show that the three pores (pores A, B and C), which are marked with red arrows in Figure 7(b), occupy about 14 % of the cross-sectional area of the fracture surfaces. Meanwhile the hard inclusions, i.e. iron-intermetallics, Al_2Cu intermetallic phase and Si particles, also occupy a large area proportion of the fracture surface. Indeed, their surface fractions in the fracture surface are higher than their respective volume fractions in bulk. A surface fraction of 12 % of Al_2Cu intermetallic phases was detected in the fracture as compared to a 1.3 % volume fraction identified from microstructure characterization. Almost 9.3 % iron-intermetallics and 28 % eutectic Si were detected in one part of the fracture surface (Figure 7(c)) as compared to, respectively, 4.0 % of iron-intermetallics measured in bulk and 7.1 % of eutectic Si measured from 2D observations on a large area ($\sim 4.4 \text{ mm}^2$).

Damaged hard inclusions include eutectic Si, iron-intermetallics and Al_2Cu intermetallic phases, which are observed in the fracture surface as shown in Figure 7(c) and (d). Decohesion (see the red arrows in Figure 7(c) and (d)) and fracture (see the blue arrows in Figure 7(c) and (d)) of iron-intermetallics are both found in cracks propagations regions, and the observations revealed that more fracture than decohesion is found in all the fracture surfaces.

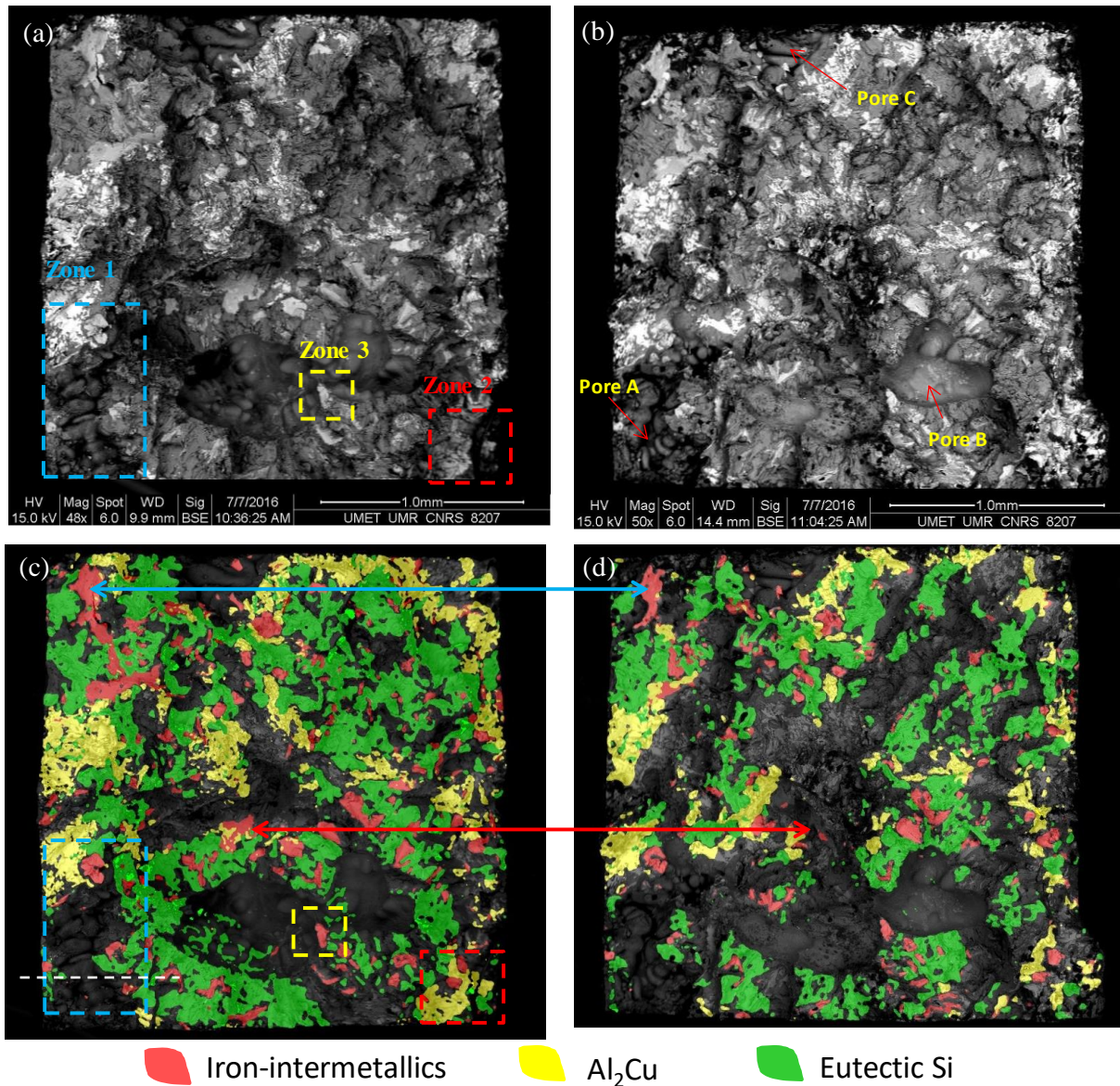


Figure 7: (a), (b) Back Scattered Electron images of the fracture surfaces and (c), (d) corresponding X-ray mapping images showing the distribution of hard inclusions (eutectic Si, iron-intermetallics, Al₂Cu intermetallic phases), (c) is upper and (d) is lower.

The difference between the reference and the deformed images, i.e. the image at the deformed state corrected by the displacement computed with DVC, is the residual error. This residual error field provides valuable information about the crack geometry as it is maximum at the crack location [25], thus all the cracks in the present study were extracted from the DVC residual errors.

The 3D rendering of cracks at the last loading step before fracture is shown with the pores and broken specimen in Figure 8. Two large cracks in black (cracks 1 and 2) were visible around pore A and near the corner of specimen, respectively. The strain field calculated by DVC at an applied stress of 187 MPa (last step before final fracture) is superimposed on the pores. A good correlation can be observed between strain localization in the measured fields and the crack 1 location. Meanwhile, another small crack, i.e. crack 3, was initiated from the corner of large subsurface Pore B. Three small subvolumes, in which these three main cracks were observed, were extracted for the following analysis to illustrate the mechanisms of crack initiation and propagation.

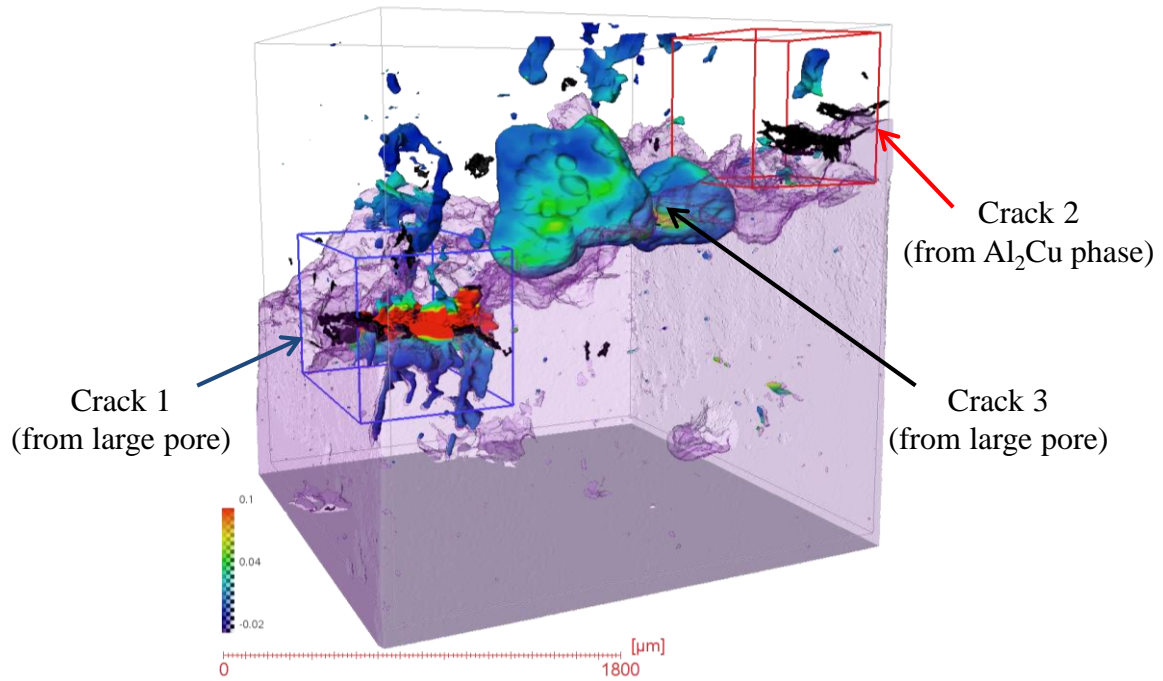


Figure 8: 3D rendering of pores and cracks (in black) with the fracture surface of studied specimen, the ϵ_{zz} strain calculated by DVC at the step before final fracture (187MPa) is superimposed on the pores

3.2.1 Crack 1

Figure 9 shows the evolution of crack 1 during the in-situ tensile test. Figure 9(a) shows that a slight strain localization was firstly observed around Pore A at an early load step (145 MPa), although no crack was visible. With increasing load, the strain localizations became more obvious both at Pore A and the nearby Al₂Cu particles, with crack 1 observed to initiate around the circumference of Pore A.

Figure 9(c) shows the 3D rendering of crack 1 at the last loading step before failure, i.e. at 187MPa, and the corresponding high strain localization in Al₂Cu intermetallic phase in front of the existing crack that matches with the final crack path. Because eutectic Si phase cannot be revealed using Lab-CT, the tomography slice that contains the crack shown in Figure 9(b) and (c) was compared to the fracture surface examined with EDS. At the slice location, which corresponds to the dotted white line in Figure 7(c) (in zone 1), eutectic Si was detected in the fracture surface. Crack 1 initiated around Pore A and went through the Al₂Cu intermetallic phase as shown in Figure 9(d); Pore A and Al₂Cu particles appear transparent. Thus, from these observations, crack 1 fractured a Si particle then advanced into an iron-intermetallic particle (Figure 7(c)) and the Al₂Cu particle shown in Figure 8.

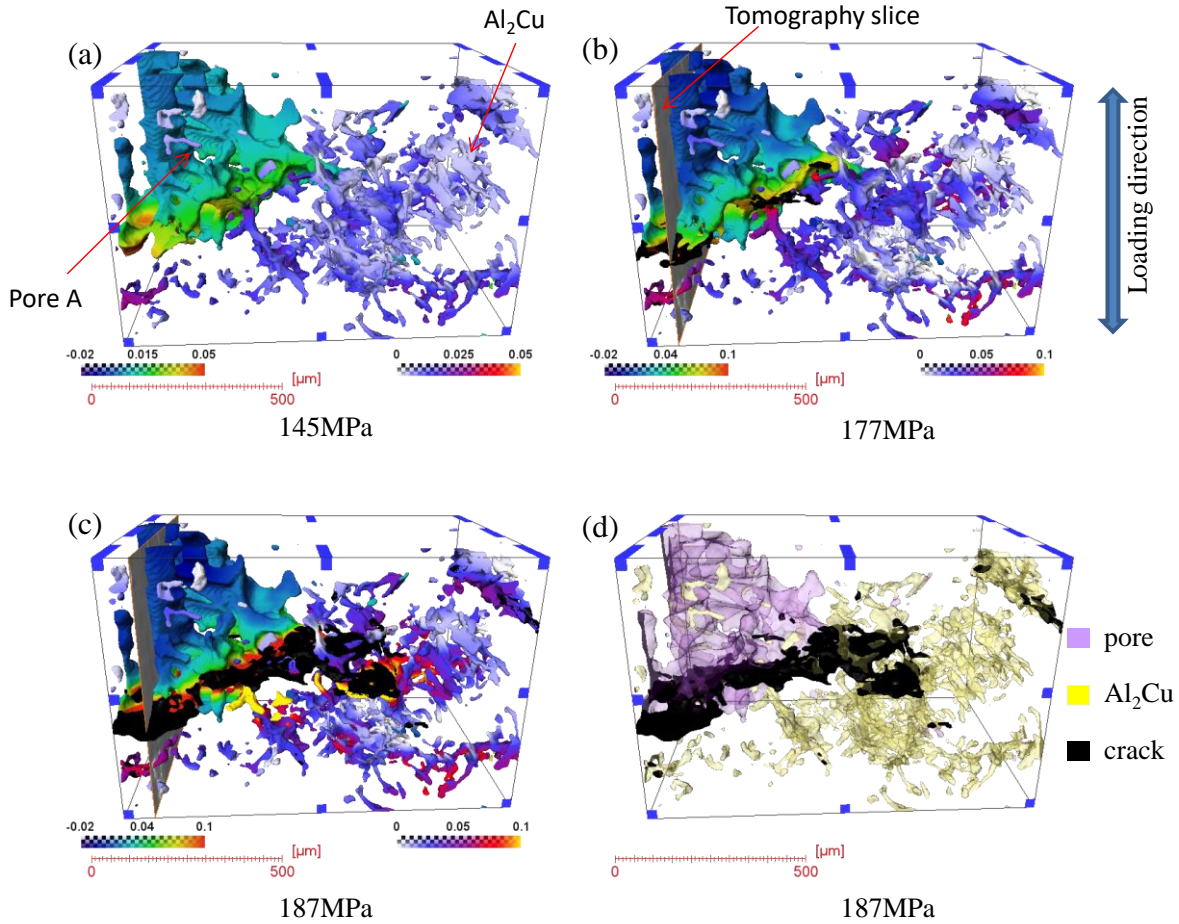


Figure 9: 3D rendering of the pore A and nearby Al₂Cu intermetallic phases on which are superimposed the ϵ_{zz} strain calculated by DVC at different applied stresses, (a) 145 MPa, (b) 177 MPa; 3D crack (in black) at the last step before final fracture (187MPa) through the Al₂Cu intermetallic phase, (c) with strain field, (d) in transparent. (the left and right colormap scales represent the ϵ_{zz} strain fields for pore and Al₂Cu intermetallic phase, respectively)

3.2.2 Crack 2

The evolution of crack 2 at different loading steps is depicted in Figure 10. The strain field was superimposed on the 3D rendering of Al₂Cu intermetallic phases in the selected volume at different loading steps before failure.

Strain localizations with a small maximum strain value appeared in the Al₂Cu intermetallic phases at an applied stress of 160 MPa (see the red arrows in Figure 10(a)). No cracks can be detected from the tomographic images at this loading step. Crack initiation was identified at an applied stress of 177 MPa and a good correlation can be observed between strain localization and the location of this crack at Al₂Cu intermetallic phase (Figure 10(b)). This confirms that the DVC strain field allows detecting the crack initiation site at an early loading step. Figure 10(c) shows strain fields on the Al₂Cu intermetallic phases for an applied stress of 187 MPa, where growth of the crack is observed. Figure 10(d) shows that crack 2 seems to mainly go through the Al₂Cu intermetallic phase close to the corner of specimen. This result is in accordance with the SEM-EDS observations, fracture of large Al₂Cu intermetallic phase can be observed in zone 2 of the fracture surface (see Figure 7(c)).

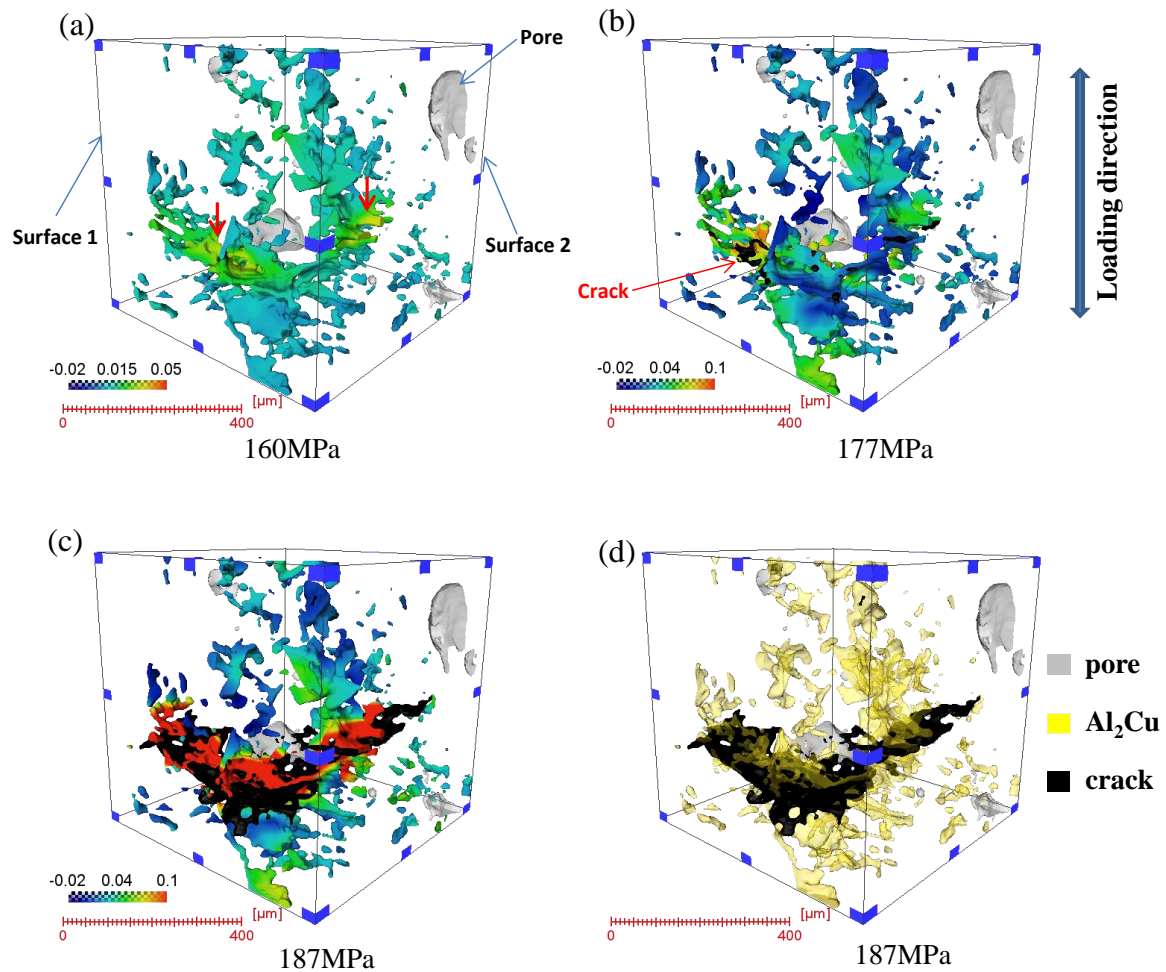


Figure 10: 3D rendering of cracks (in black) and Al_2Cu intermetallic phases on which are superimposed the ϵ_{zz} strain calculated by DVC at different applied stresses: (a) 160 MPa, (b) 177 MPa, 3D crack (in black) at the last step before final fracture (187MPa) through the Al_2Cu intermetallic phase, (c) with strain field, (d) in transparent.

3.2.3 Crack 3

Figure 11(a) and (b) show the strain field at an applied stress of 150 MPa along the loading direction; the 3D rendering of pore B and the nearby iron-intermetallic were superposed to this field to allow comparison between the evolution of the crack and local deformation. Strain localization is observed in the α -iron intermetallic phase, which is located on the corner of the pore B, although no crack can be detected at this loading step.

The strain value at this point was observed to increase at increasing load until crack initiation at an applied stress of 160 MPa. However, once the crack became visible in the α -iron-intermetallic phase, it grew very slowly. In Figure 11(c) where crack 3 is represented in red and the strain field was superimposed on the pore at the last step before the final fracture, a good correlation is observed between the crack location at 187MPa and the strain localization at 150MPa. Figure 11(d) shows the tomographic slice where crack 3 initiated in the α -phase. The fracture of this α -phase can also be identified from the SEM-EDS analysis of the fracture surface (see the yellow dotted box “zone 3” in Figure 7(c)).

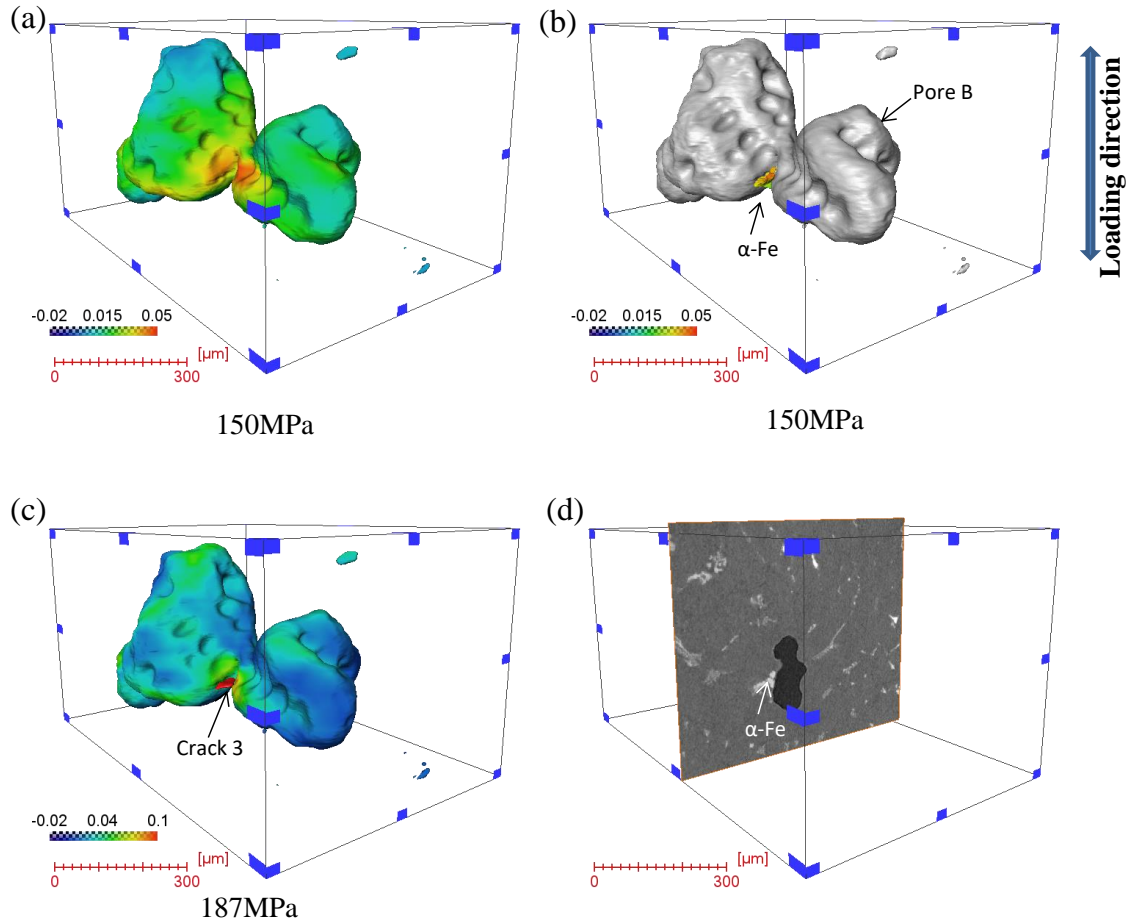


Figure 11: 3D rendering of (a) pore B close to (b) an iron-intermetallic on which is superimposed the ϵ_{zz} strain calculated by DVC at an applied stress of 150MPa. (c) 3D rendering of crack 3 (in red) with the pore B on which is superimposed the strain field before the final fracture. (d) One tomographic slice shows the location of iron-intermetallic

3.3 Quantitative analysis

As shown in section 3.2, strain localizations were observed at an early load step in the regions where crack initiation was later observed. Thus, the strain evolution at cracked particles until failure can be quantitatively assessed by DVC.

In this work, particles analyses with DVC were made in order to determine the strain behaviour of Al_2Cu intermetallic phase and iron-intermetallic. The local values determined from the analysis of strain fields obtained with YaDICs depend on the selected point locations (12 points were selected on each phase).

Figure 12 illustrates the comparison between the DVC element size ($8 \times 8 \times 8$ voxels³ i.e. $24 \times 24 \times 24 \mu\text{m}^3$) and the size of selected particles. The von Mises' equivalent strain field measured at the last load step before final fracture is superimposed on the tomographic image. The selected points, which are inside the subset, are shown. However, the element size, which is represented in 2D here, has an edge three times smaller than the true spatial resolution of strain. Here, the ϵ_{zz} strain in one given element is actually computed as the gradient of displacement between the element above and the element below. As a result, even when one element contains a single phase, the measured strain inside the element/phase is an average between the matrix and the particles. Nevertheless, the measured strain value in the selected particles can give a rough estimate of differences in strain behaviour of Al_2Cu intermetallic phase and iron-intermetallics.

The evolution of von Mises' equivalent strain in the selected particles (Al_2Cu -1 to Al_2Cu -12 and Fe-intermetallic-1 to Fe-intermetallic-12) as a function of load is shown in Figure 13. The strain local values increase with increasing load up to their failure. The particles once broken are not shown in the Figure. The average local strain levels that lead to the cracking of particles are about 4.5 ± 1.0 % (standard deviation) for the Al_2Cu intermetallic phase and 3.5 ± 1.1 % for the iron-intermetallics. These strain values are to be taken with caution due to the large uncertainty in the present study; this large uncertainty compared to [20] may result from less microstructural features than what can be observed with synchrotron tomography.

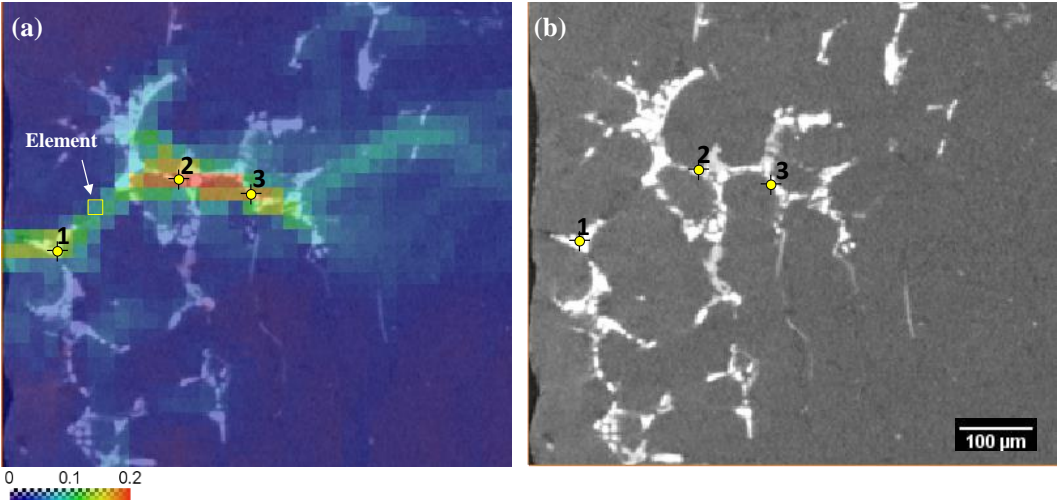


Figure 12 : Comparison of DVC element size in the von Mises' equivalent strain field with the size of the selected particles

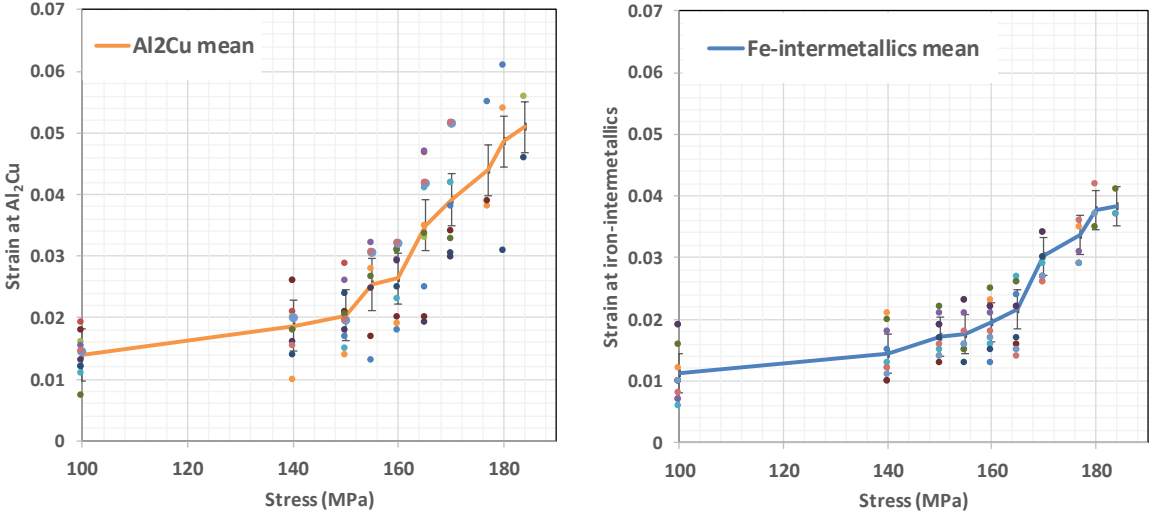


Figure 13 : Evolution of the von Mises' equivalent strain value in some Al_2Cu particles (on the left) and some iron-intermetallic particles (on the right) before fracture during the tensile test; dot symbols with different colours stand for different particles.

4 Discussion

4.1 Damage mechanisms (3D tensile damage mechanisms)

This study revealed that the crack path under monotonic tensile loading in LFC A319 alloy with solution heat treatment is sensitive to microstructure. All the main cracks and the final fracture occurred in the selected ROI where the largest strains were computed with FEM simulation of the porous specimen. Undoubtedly, large pores play the most important role in the failure of specimens. However, the hard inclusions, which are located in the vicinity of the large pores, may also have an influence on the damage mechanisms.

Due to the stochastic distribution of hard inclusions within the alloy, although the total volume fraction of Al_2Cu intermetallic phase decreased after the heat treatment, the local volume fraction in the heat-treated specimen may surpass the average volume fraction in the as cast specimen. Comparison of the volume fraction of Al_2Cu intermetallic phase between a large volume (DVC subvolume) and one small subvolume, which includes the critical pores (i.e. pore A, B and C), cracks and final fracture of the specimen, is summarized in Table 3.

The volume fraction of Al_2Cu (1.4 %) in the selected small subvolume is higher than that of a large volume (DVC subvolume) of the heat-treated specimen (0.66 %); It is even close to that of the as-cast sample (1.6 %), the reason is that the selected analysis subvolume is too small to be representative of the sample volume. Thus, the results presented here are not representative for the influence of heat treatment on the damage mechanisms of LFC A319 alloy. Despite all this, we can develop a better understanding of the damage mechanisms involved in the studied alloy.

Table 3 : Quantitative analysis of Al_2Cu intermetallic phase in the studied specimen (Note: 1. Volume of DVC subvolume =10.58 mm³ 2. Volume of subvolume=1.2 mm³ 3. Fracture surface=4 mm²)

Before heat treatment		After heat treatment	
Vol. fraction% (DVC subvolume) ¹	Vol. fraction% (ROI) ¹	Vol. fraction % (subvolume) ²	Surf. fraction % (fracture surface) ³
1.60	0.66	1.40	11.6

4.2 Crack initiation

3D in-situ tensile testing coupled with DVC analysis revealed the dominant influence of pores on strain localization and crack initiation in LFC A319 alloy. In all the tensile tests, most of the cracks initiated around large pores, and the size, location and shape of a pore were found to influence crack initiation during tensile testing.

In the studied specimen, cracks initiated from the surface shrinkage Pore A (volume: 0.0177 mm³) rather than from the smaller surface shrinkage Pore C (volume: 0.0037 mm³), which proves that the size of the pore is an important factor.

Numerous researchers have reported the effect of pore size on crack initiation [6,26,27] in alloys that were not cast with lost foam casting, which introduces some large defects. There exists some critical pore size in the range of 25 to 50 μm for fatigue crack initiation in Sr modified cast A356 alloy [27]; below this size, cracks initiate from other microstructural features such as eutectic particles and slip bands. In the present study, cracks were found to initiate at large pores (Pore A), which are apt to induce stress concentration during tensile loading.

In addition, cracks in LFC A319 alloy were found to initiate preferentially close to large shrinkage pores rather than round gas pores. For example, cracks initiated from shrinkage Pore A (sphericity: 0.078).

These pores act as preferred crack nucleation sites because of the high stress concentration at the sharp radius of curvature that makes them morphologically crack-like [28].

One can also note that the small crack 3 was located on corner of the Pore B (volume: 0.098 mm³, sphericity: 0.42). This might be because the corner of the pore B has a sharp radius of curvature hence a higher stress concentration or a high strain localization as observed in the DVC strain field; the complex morphology of the pores has thus a significant influence on the local stress concentrations hence on the crack initiation process.

The location of pores is also an important factor. As shown in Figure 6, some shrinkage pores are located inside the specimen. However, no cracks can be detected at them. Indeed, [22] reported that the preferred sites for crack initiation are pores located at or near the surface of the specimen. We can propose that the relatively high stress concentration at pores, particularly surface pores, is responsible for strain localization leading to crack initiation. Therefore, morphology and location are two important factors for cracks initiation as the large surface shrinkage pore was more dangerous than the larger subsurface round pore.

In addition, experimental evidence indicates that tensile failures of the studied LFC A319 alloy often initiate at hard inclusions, i.e. eutectic Si, Al₂Cu intermetallic phase and iron-intermetallic, that are located around large pores or near the surface of specimen rather than at Al matrix. Hence, cracks 1 and 3 were observed to initiate around the largest Pore A at eutectic Si and α -Al_x(Fe,Mn)_ySi phase, respectively. Meanwhile, Al₂Cu intermetallic phase acted as another crack nucleation site (crack 2) in the absence of large pores but at a sharp corner where stress concentration is easy to generate.

In general, the presence of large pores or/and the specimen geometry will result in stress concentration in the surrounding matrix and at hard inclusions. However, hard inclusions have a higher elastic modulus and are more fragile than Al matrix [29]. Besides, as characterized previously, they have locally sharp morphologies compared to the Al matrix, thus, a larger stress concentration is easier to generate at hard inclusions than elsewhere in Al matrix and crack initiation occurs very rapidly by rupture of this particle. [21] explains that hard inclusions are prone to cracking during mechanical loading because of the strain incompatibility between the aluminium matrix, which has an elasto-viscoplastic behaviour, and hard inclusions (particularly Si particles). The acicular eutectic Si particles, which are brittle, serve as a bridge for crack propagation. Although the studied alloy was slightly modified with ~120ppm of Sr and solution treated for 50 h at 495°C, Si particles were still large and interconnected into a network, which may show high stress concentration factors [28]. In the literature [30,31] on Al-Si-Cu alloys, crack initiation was observed to occur through the fragmentation of Si particles, iron intermetallics (especially for platelets-like β -phase), as well as Al₂Cu particles.

Moreover, as discussed before, the hard inclusions close to large pores have an important influence on the damage mechanisms. Although the studied specimen was subjected to heat treatment, a high volume fraction of Al₂Cu (1.4 %) was found in the subvolume that contains large pores. Crack were found to initiate from Al₂Cu intermetallic phase at a sharp edge of the specimen where stress concentration is prone to occur. This confirms that the volume fraction of hard inclusions, here Al₂Cu, in the vicinity of large pores is also an important factor that dictates the most likely cracks initiation sites.

4.3 Crack growth and final fracture

After cracks have initiated at hard inclusions in the areas with high enough stress concentration, they went on growing along the hard inclusions.

As discussed in section 3.2, 3D analysis of crack evolution revealed that crack growth was prone to occur along the hard inclusions including eutectic Si phase, iron intermetallics and Al₂Cu intermetallic phases. This can be ascribed to strain build-up at these hard inclusions with an increasing applied stress. Indeed, strain localizations occurred in areas where cracks growths were observed in the following loading step.

A tomographic slice, located about 850 μm below the flat surface of the specimen, is shown with 3D rendering of cracks and fracture surface in Figure 14(a). This slice is located away from the tip of the main cracks. The strain field (Figure 14(b)) in the same slice at the last loading step is shown translucent and superimposed onto the tomographic slice to highlight the relation between strain localization at hard inclusions and final failure. It is impossible to know if there are microcracks at all the strain localizations areas due to the limited resolution of tomographic images (voxel size=3 μm). However, the final failure path (red line marked in Figure 14(b)) went through the areas where strain localizations are marked by white dotted circles. Consequently, hard inclusions play an important role in strain distribution hence affecting crack propagation and final fracture.

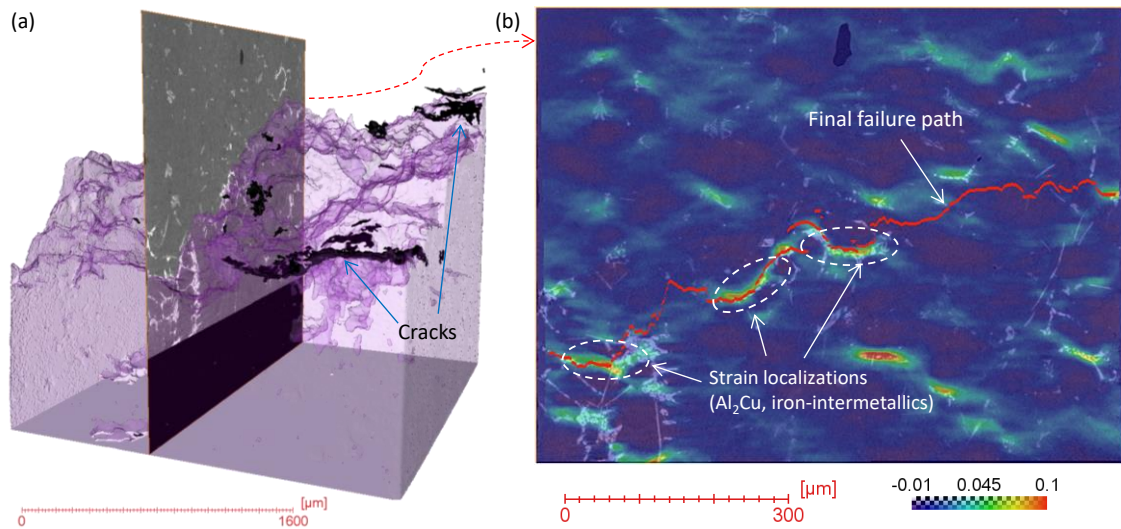


Figure 14: (a) One slice (about 850 μm below the flat surface) shown with a 3D rendering of cracks in black (at last loading step before failure) and fracture surface of the specimen in purple, (b) strain field of this slice in the last loading step before failure

Post-mortem observations also revealed the role of hard inclusions, i.e. eutectic Si, Al₂Cu intermetallic phase and iron-intermetallic, in the crack growth and final fracture process. Looking at the SEM-EDS observations in Figure 7, whether one considers cracks initiation, cracks propagation or final fast fracture, they are all more likely to occur along hard inclusions. Comparison of phases' surface fraction between fracture surfaces and sub-volume or flat surfaces of the specimen shows that the amount of eutectic Si particles, iron intermetallic phases and Al₂Cu intermetallic phases is higher in the fracture surfaces than elsewhere in the specimen. The ratio of Al₂Cu and iron-intermetallic phases fraction between surface fraction on the fracture surface and the volume fraction in the subvolume close to the final fracture are 8.6 and 2.2, respectively; for eutectic Si, the ratio between surface fraction on fracture surface and that on the flat surface is 3.9.

As a result, cracks and final fracture are more prone to occur at hard inclusions than in Al dendrites. This may be due to the elastic modulus of eutectic Si particles (185 GPa), iron-intermetallics (166-180 GPa) and Al₂Cu intermetallic phases (126 GPa) which are higher than that of the aluminium matrix (92 GPa). This elastic modulus mismatch can introduce incompatibility of deformation between the hard inclusions and the aluminium matrix, thus they are reported to play a role in crack propagation as a preferential path [28]. Besides, comparison of phases distribution between both fracture surfaces of the same specimen reveals that more fracture than decohesion of hard inclusions is found.

[32] showed that fracture of Si particles is the dominant mechanism in an unmodified Al-Si-Mg alloy with large (~3-9 μm) Si particles during the fatigue test. In contrast, decohesion of Si particles from the Al-matrix always occurs in the smaller Si particles. In the present work, the average size of Si particles is larger than 10 μm . This can be one of the reasons why more fracture than decohesion is detected in the fracture surface.

Furthermore, the high level of applied load in tensile test can also affect the damage mechanism of hard inclusions. [33] deduced that debonding of Si particles dominates the fatigue crack growth process at a maximum stress intensity factor, K_{\max} , below $6 \text{ MPa}\sqrt{\text{m}}$, but fracture of Si particles dominates at K_{\max} above $6 \text{ MPa}\sqrt{\text{m}}$. In our study, the specimens were subjected to high stress in monotonic tension up to failure so that the Si particles fracture rather than debond.

The present work demonstrates that more fracture than decohesion is found in iron intermetallics and Al_2Cu intermetallic phases. In Al-Si alloy castings, cracks are reported to appear within the $\beta\text{-Al}_5\text{FeSi}$ platelets rather than at the β/Al interface [31]. This is due to the brittle nature of the β -phase, where the platelets are easily split into two halves. The cracks propagation through the fracture of undissolved Al_2Cu [31] is consistent with our observations.

4.4 Strain measurements and crack formation

Strain measurements by DVC coupled with the observation of 3D crack evolution indicated that in-situ tensile tests under Lab-CT analyzed with DVC technique can successfully be used to quantify the 3D spatial and temporal strain patterns for the studied alloy. DVC is able to monitor the deformation at the microstructure level during the tensile test. The quantitative DVC analysis highlights the possibility to understand the roles of the various hard inclusions (Al_2Cu intermetallic phase and iron-intermetallic) on the damage mechanisms of LFC A319. The average local strain level that leads to the cracking of iron-intermetallic is lower than that for Al_2Cu . The higher elastic modulus (166-180 GPa) of iron-intermetallics in comparison with that of Al_2Cu intermetallic phases (126 GPa) [34] could indeed lead to the cracking of iron-intermetallics at a lower strain than for Al_2Cu .

A quantitative assessment of the local material response prior to crack initiation was performed on the studied specimens. With an accurate assessment of strain localization prior to crack formation, the locations of potential tensile cracks and their severity can be understood.

5 Conclusions

The usefulness of 3D in-situ tensile tests under X-ray tomography coupled with digital volume correlation (DVC) to study the damage mechanism of LFC A319 alloys has been proved. To the best of the author's knowledge, it is the first time that the evolution of the local strain at hard inclusions before fracture was measured during a tensile test. The localization of strain at the microstructural level prior to crack formation determines the location of micro-cracks which form later during the tensile loading.

In addition, post-mortem analyses were performed using SEM and EDS on flat surfaces and fracture surfaces; they helped identifying final failure, micro-cracks, crack initiation zone and thus allowed the damage mechanisms to be thoroughly understood.

For the studied LFC A319 alloy, the tensile damage mechanisms can be summarized as:

1. Cracks initiate at hard inclusions in the areas with sufficient stress concentrations, which are mainly provided by large pores. The different size, location and shape of pores result in different stress concentrations. Therefore, they affect the cracks initiations during the tensile test. For example, large shrinkage pores located at or near the surface of the specimen more easily introduce stress concentrations than small rounded gas pores within the interior, thus they provide crack initiation sites.
2. The large pores can decrease the effective bearing area in the plane perpendicular to the loading direction, and introduce large stress concentration during the tensile test. Consequently, cracks can initiate at hard inclusions near the pores. Then, with the load increase, cracks can also initiate at hard inclusions (i.e. Al_2Cu intermetallic phase and eutectic Si) located in the same plane as pores, away from the pores but close to the surface of specimen.
3. The presence of large pores or/and specimen geometry will result in stress concentration in the surrounding matrix and hard inclusions during tensile test. Hard inclusions can act as crack

initiation sites due to their higher elastic modulus and because they are more fragile than Al matrix.

4. The quantitative analysis revealed that the iron-intermetallics show a lower average strain level for the cracking of particle than Al₂Cu intermetallic phase.
5. Once cracks initiated, they prefer to grow through the cracked hard inclusions, i.e. eutectic Si, iron intermetallics and Al₂Cu intermetallic phase. The fast final fracture is more prone to occur at Si phase, iron intermetallics and Al₂Cu intermetallic phases than in Al dendrites. In a tensile test, more fracture of hard inclusions is observed than decohesion whether in cracks initiation region, cracks propagation region or final fast fracture region.

6 Acknowledgements

This research work was funded by the ANR (Agence Nationale de la Recherche) MatetPro project INDiANA. The authors would like to thank ISIS4D (<https://isis4d.univ-lille.fr/>) X-Ray CT platform (Lille, France) and Grégory Hauss (LaMcube laboratory) for the use of in-situ tensile test set-up; The ISIS4D X-Ray CT platform has been funded by International Campus on Safety and Intermodality in Transportation (CISIT), the Nord-Pas-de-Calais Region, the European Community and the National Center for Scientific Research. The authors gratefully acknowledge the support of these institutions. The PSA Peugeot Citroën is also acknowledged for providing the material; Pierre Osmond from PSA is particularly acknowledged for performing the solution heat treatment. The authors are also grateful to the China Scholarship Council (CSC) for funding the PhD thesis of Zaidao Li.

7 Data Availability Statement

All relevant data used to support the findings of this study are available from the corresponding author upon request.

References

- [1] R. González, D.I. Martinez, J.A. González, J. Talamantes, S. Valtierra, R. Colás, Experimental investigation for fatigue strength of a cast aluminium alloy, *Int. J. Fatigue*. 33 (2011) 273–278.
- [2] N. Limodin, A. El Bartali, L. Wang, J. Lachambre, J.-Y. Buffiere, E. Charkaluk, Application of X-ray microtomography to study the influence of the casting microstructure upon the tensile behaviour of an Al–Si alloy, *Nucl. Instruments Methods Phys. Res. Sect. B Beam Interact. with Mater. Atoms*. 324 (2014) 57–62.
- [3] S. Tabibian, E. Charkaluk, A. Constantinescu, A. Oudin, F. Szymtka, Behavior, damage and fatigue life assessment of lost foam casting aluminum alloys under thermo-mechanical fatigue conditions, *Procedia Eng.* 2 (2010) 1145–1154.
- [4] I. Serrano Munoz, Influence of casting defects on the fatigue behaviour of an A357-T6 aerospace alloy, Lyon, INSA, 2014.
- [5] I. Boromei, L. Ceschini, A. Morri, G. Nicoletto, E. Riva, Influence of the solidification microstructure and porosity on the fatigue strength of Al-Si-Mg casting alloys, *Metall. Sci. Technol.* 28 (2010).
- [6] L. Wang, N. Limodin, A. El Bartali, J.F. Witz, R. Seghir, J.Y. Buffiere, E. Charkaluk, Influence of pores on crack initiation in monotonic tensile and cyclic loadings in lost foam casting A319 alloy by using 3D in-situ analysis, *Mater. Sci. Eng. A*. 673 (2016) 362–372. doi:10.1016/j.msea.2016.07.036.
- [7] Z. Li, N. Limodin, A. Tandjaoui, P. Quaegebeur, J.F. Witz, D. Balloy, Influence of Fe content on the damage mechanism in A319 aluminum alloy: Tensile tests and digital image correlation, *Eng. Fract. Mech.* 183 (2017) 94–108. doi:10.1016/j.engfracmech.2017.05.006.
- [8] M.D. Dighe, A.M. Gokhale, Relationship between microstructural extremum and fracture path in a cast Al-Si-Mg alloy, *Scr. Mater.* 37 (1997).
- [9] A. Mocellin, Y. Brechet, R. Fougères, Fracture of an osprey™ AlSiFe alloy: A microstructure

- based model for fracture of microheterogeneous materials, *Acta Metall. Mater.* 43 (1995) 1135–1140.
- [10] S. Joseph, S. Kumar, V.S. Bhadram, C. Narayana, Stress states in individual Si particles of a cast Al–Si alloy: micro-Raman analysis and microstructure based modeling, *J. Alloys Compd.* 625 (2015) 296–308.
- [11] B. Cantor, G.A. Chadwick, The tensile deformation of unidirectionally solidified Al–Al 3 Ni and Al–Al 2 Cu eutectics, *J. Mater. Sci.* 10 (1975) 578–588.
- [12] Z. Li, N. Limodin, A. Tandjaoui, P. Quaegebeur, P. Osmond, D. Balloy, Influence of Sr, Fe and Mn content and casting process on the microstructures and mechanical properties of AlSi7Cu3 alloy, *Mater. Sci. Eng. A.* 689 (2017) 286–297.
- [13] S. Shivkumar, S. Ricci, C. Keller, D. Apelian, Effect of solution treatment parameters on tensile properties of cast aluminum alloys, *J. Heat Treat.* 8 (1990) 63–70.
- [14] M.A. Moustafa, F.H. Samuel, H.W. Doty, Effect of solution heat treatment and additives on the microstructure of Al–Si (A413. 1) automotive alloys, *J. Mater. Sci.* 38 (2003) 4507–4522.
- [15] H. Toda, T. Nishimura, K. Uesugi, Y. Suzuki, M. Kobayashi, Influence of high-temperature solution treatments on mechanical properties of an Al–Si–Cu aluminum alloy, *Acta Mater.* 58 (2010) 2014–2025.
- [16] A.M.A. Mohamed, F.H. Samuel, A review on the heat treatment of Al–Si–Cu/Mg casting alloys, in: *Heat Treat. Nov. Appl.*, IntechOpen, 2012.
- [17] H. Toda, I. Sinclair, J.-Y. Buffiere, E. Maire, K.H. Khor, P. Gregson, T. Kobayashi, A 3D measurement procedure for internal local crack driving forces via synchrotron X-ray microtomography, *Acta Mater.* 52 (2004) 1305–1317.
- [18] H. Toda, S. Yamamoto, M. Kobayashi, K. Uesugi, H. Zhang, Direct measurement procedure for three-dimensional local crack driving force using synchrotron X-ray microtomography, *Acta Mater.* 56 (2008) 6027–6039.
- [19] H. Toda, E. Maire, S. Yamauchi, H. Tsuruta, T. Hiramatsu, M. Kobayashi, In situ observation of ductile fracture using X-ray tomography technique, *Acta Mater.* 59 (2011) 1995–2008.
- [20] N. Dahdah, N. Limodin, A. El Bartali, J.-F. Witz, R. Seghir, E. Charkaluk, J.-Y. Buffiere, Damage Investigation in A319 Aluminium Alloy by X-ray Tomography and Digital Volume Correlation during In Situ High-Temperature Fatigue Tests, *Strain.* 52 (2016) 324–335.
- [21] S. Dezecot, J.-Y. Buffiere, A. Koster, V. Maurel, F. Szmytka, E. Charkaluk, N. Dahdah, A. El Bartali, N. Limodin, J.-F. Witz, In situ 3D characterization of high temperature fatigue damage mechanisms in a cast aluminum alloy using synchrotron X-ray tomography, *Scr. Mater.* 113 (2016) 254–258.
- [22] L. Wang, Influence of the casting microstructure on damage mechanisms in Al–Si alloys by using 2D and 3D in-situ analysis, *Ecole Centrale de Lille*, 2015.
- [23] R. Seghir, J.-F. Witz, S. Coudert, YaDICS-Digital Image Correlation 2/3D software, (2014). <http://www.yadics.univ-lille1.fr>.
- [24] Z. Li, N. Limodin, A. Tandjaoui, P. Quaegebeur, J.-F. Witz, D. Balloy, Damage investigation in A319 aluminum alloy by digital image correlation during in-situ tensile tests, *Procedia Struct. Integr.* 2 (2016) 3415–3422. doi:10.1016/J.PROSTR.2016.06.426.
- [25] N. Limodin, J. Réthoré, J.-Y. Buffière, A. Gravouil, F. Hild, S. Roux, Crack closure and stress intensity factor measurements in nodular graphite cast iron using three-dimensional correlation of laboratory X-ray microtomography images, *Acta Mater.* 57 (2009) 4090–4101.
- [26] P. Mu, Y. Nadot, C. Nadot-Martin, A. Chabod, I. Serrano-Munoz, C. Verdu, Influence of casting defects on the fatigue behavior of cast aluminum AS7G06-T6, *Int. J. Fatigue.* 63 (2014) 97–109.
- [27] Q.G. Wang, D. Apelian, D.A. Lados, Fatigue behavior of A356-T6 aluminum cast alloys. Part I. Effect of casting defects, *J. Light Met.* 1 (2001) 73–84.
- [28] K.S. Chan, P. Jones, Q. Wang, Fatigue crack growth and fracture paths in sand cast B319 and A356 aluminum alloys, *Mater. Sci. Eng. A.* 341 (2003) 18–34.
- [29] C.-L. Chen, A. Richter, R.C. Thomson, Investigation of mechanical properties of intermetallic phases in multi-component Al–Si alloys using hot-stage nanoindentation, *Intermetallics.* 18 (2010) 499–508.
- [30] I. Bacaicoa, P.K. Dwivedi, M. Luetje, F. Zeismann, A. Brueckner-Foit, A. Geisert, M. Fehlbier, Effect of non-equilibrium heat treatments on microstructure and tensile properties of an Al–Si-

- Cu alloy, *Mater. Sci. Eng. A.* 673 (2016) 562–571.
- [31] Z. Ma, A.M. Samuel, H.W. Doty, S. Valtierra, F.H. Samuel, Effect of Fe content on the fracture behaviour of Al – Si – Cu cast alloys, *Mater. Des.* 57 (2014) 366–373. doi:10.1016/j.matdes.2014.01.037.
- [32] F.T. Lee, J.F. Major, F.H. Samuel, Effect of silicon particles on the fatigue crack growth characteristics of Al-12 Wt Pct Si-0.35 Wt Pct Mg-(0 to 0.02) Wt Pct Sr casting alloys, *Metall. Mater. Trans. A.* 26 (1995) 1553–1570.
- [33] K. Gall, N. Yang, M. Horstemeyer, D.L. McDowell, J. Fan, The debonding and fracture of Si particles during the fatigue of a cast Al-Si alloy, *Metall. Mater. Trans. A.* 30 (1999) 3079–3088.
- [34] S. Tabibian, E. Charkaluk, A. Constantinescu, G. Guillemot, F. Szymtka, Influence of process-induced microstructure on hardness of two Al–Si alloys, *Mater. Sci. Eng. A.* 646 (2015) 190–200.